



## An energy analyzing detector for cold neutrons

N.C. Maliszewskyj<sup>a,\*</sup>, A. Osovizky<sup>a,b,c</sup>, K. Pritchard<sup>a</sup>, Y. Yehuda-Zada<sup>c</sup>, E. Binkley<sup>a</sup>,  
J. Ziegler<sup>a</sup>, P. Tsai<sup>a</sup>, N. Hadad<sup>a</sup>, G.M. Baltic<sup>a</sup>, M. Jackson<sup>d</sup>, C. Hurlbut<sup>d</sup>, C.F. Majkrzak<sup>a</sup>

<sup>a</sup> NIST Center for Neutron Research, Gaithersburg, MD, 20899, USA

<sup>b</sup> Rotem Industries Ltd, Rotem Industrial Park, 86800, Israel

<sup>c</sup> Nuclear Research Center Negev, Beer-Sheva, 61070, Israel

<sup>d</sup> Eljen Technology, Sweetwater, TX, 79556, USA

### ARTICLE INFO

#### Keywords:

Neutron detector  
LiF:ZnS(Ag)  
Scintillator  
CANDoR

### ABSTRACT

We describe the design, fabrication, and performance of an energy analyzing detector package for cold neutron spectrometers at the NIST Center for Neutron Research (NCNR). The detector package consists of arrays of highly oriented pyrolytic graphite crystals set at takeoff angles corresponding to different neutron energies. Neutrons incident down the array will be selected out by the appropriate crystal and directed onto an associated neutron detector. The arrays are capable of binning neutrons into one of 54 bins over an energy range of 2.29 meV to 5.11 meV.

We describe theory of operation, the development of a highly efficient ultrathin neutron sensor, and the development of the arrays themselves. We present preliminary results for this detector array along with a mature design of the scintillator neutron detector. We also present enhancements we are pursuing prior to deployment of this technology.

### 1. Introduction

Canonical neutron scattering instruments at continuous sources have typically operated around a monoenergetic beam of neutrons selected from the source spectrum via crystal monochromators or mechanical selectors. Neutrons scattered from the sample are collected by a neutron detector. As the detectors are insensitive to the energy of the neutron entering them, any energy analysis is performed using crystal monochromators, filters, or time of flight techniques. The upshot is that most of the usable neutrons produced by the source are discarded (Fig. 1). Furthermore, for techniques like reflectometry in which the signal decays rapidly over at least eight decades, it can take a great deal of time to accumulate signal with statistical accuracy where it is the weakest.

The Chromatic Analysis Neutron Diffractometer or Reflectometer (CANDoR) [1] is a form of white (polychromatic) beam spectrometer in which neutrons scattered from the sample will be energy analyzed by a multi-crystal detector. Scattered neutrons will pass through an array of highly ordered pyrolytic graphite (HOPG) crystals set off at different angles with respect to the centerline of the array. Neutrons of energies corresponding to the Bragg condition for a crystal will be diffracted out towards a neutron sensitive scintillator detector. By

collecting the scattered radiation into energy bins simultaneously it will be possible to perform measurements 50 times faster using the 54-analyzer array than is currently possible with a single analyzer crystal on a conventional instrument. In specular neutron reflectometry, several such multiple analyzer arrays over a range of reflected beam angles can be implemented simultaneously, resulting in even great gains in efficiency.

To achieve this speed of measurement (and to more efficiently use the neutrons produced by our reactor), it is essential to have as many of these energy-analyzing channels as possible packed into a tight angular range. If the neutron detector is exceedingly thin (~2 mm), the spectrometer can accommodate many channels in its detector package.

### 2. HOPG array

Much like the analyzer arm of a triple axis spectrometer, the detector uses wavelength analyzer crystals and neutron detectors, but it does so using a large number of individual components [2]. The detector array consists of a series of analyzer crystals and associated independent neutron detectors assembled into a single channel for each scattering angle, shown schematically in Fig. 2. Within each array, the lowest energy (longest wavelength, blue in the schematic) neutrons are first

\* Corresponding author.

E-mail address: [nicholas.maliszewskyj@nist.gov](mailto:nicholas.maliszewskyj@nist.gov) (N.C. Maliszewskyj).

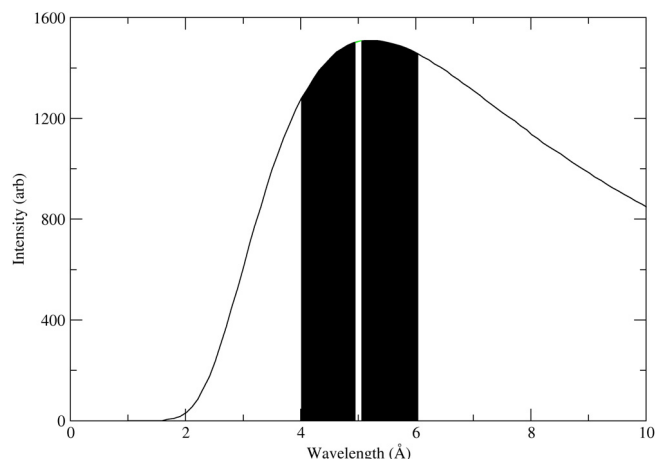


Fig. 1. Schematic cold neutron flux using a Maxwell–Boltzmann distribution at 20 K. The black area represents the neutron flux subtended by the detector for an incident white beam as compared with the flux selected by a monochromatic instrument at 5 Å.

selected while allowing the higher energy (shorter wavelength, red in the schematic) neutrons to continue down the axis of the channel to subsequent analyzers.

The analyzer crystals used to select out nearly monochromatic, narrow wavelength bands by the Bragg diffraction process are highly ordered pyrolytic graphite (HOPG) (ZYA grade manufactured by Panasonic). The thickness of each crystal is nominally 1 mm ( $\pm 10\%$ ). HOPG is characterized as an ideally imperfect mosaic crystal and is the most commonly used monochromating crystal in neutron scattering research [3,4]. HOPG consists of perfect microcrystallites (with dimensions of the order of 1  $\mu\text{m}$  to 10  $\mu\text{m}$ ) with their (002) atomic planes nearly parallel to the nominal reflecting surface (but within this plane, the crystallites are randomly oriented). The angular distribution of the (002) normals of these so-called mosaic blocks is approximately Gaussian with a full width at half maximum (FWHM) typically about half a degree. The pieces that are used in the energy-dispersive detector described herein were examined on the MAGIK neutron reflectometer at the NCNR using a perfect single crystal Si analyzer with a highly monochromatic and collimated beam (fractional wavelength resolution  $\Delta\lambda/\lambda \sim 0.01$  and  $0.04^\circ$  angular divergence, respectively). It was found that the peak reflectivity for all of the HOPG pieces in a random sampling was  $(97.0 \pm 0.5)\%$ . The full width at half maximum (FWHM) of the mosaic distribution of these crystals was found to be relatively uniform and equal to approximately  $(0.35 \pm 0.05)$  degrees.

The size of the channel is 10 mm wide by 30 mm tall. The 54 individual analyzer crystals are mounted vertically in series on an

aluminum bar with slots (several mm deep) cut to hold the bottom ends in a vice-like clamp with a set screw (placed below the neutron beam cross section). The slots are parallel to the crystal faces, beginning at an angle between the crystal face and the incoming beam direction of approximately  $63.5^\circ$  for neutrons of 6 Å nominal wavelength (this longest wavelength corresponds to the lowest wavevector transfer  $Q$  — where, for a typical sample under study the reflectivity signal is highest). From this first crystal each successive crystal is set at an angle  $0.5^\circ$  less than its predecessor down to the last crystal (downstream) which is at an angle of about  $36.5^\circ$  to reflect out neutrons of 4 Å nominal wavelength (corresponding to the highest sample  $Q$  where the background is generally the greatest). The slots are only several mm in width so that precise and accurate cutting is better accomplished with a radial saw cutting tool or by EDM (electron discharge machining). The angle of each slot has a tolerance within  $0.05^\circ$  which is of the order of 15% of the crystal mosaic width.

It was found that a laser reflected off the graphite crystal faces onto a screen approximately 7.276 m away produced a spot which could be resolved to within about 0.635 cm or  $0.05^\circ$  in angle — enough to confirm proper angular orientation of the crystals within the machine cut slots in the aluminum support bar. The fractional wavelength resolving power of each individual HOPG crystal is of the order of 1% — any misalignment of a crystal from its calculated angular position causes a nonuniform overlap onto the wavelength acceptance bands of neighboring crystals and should be minimized. Nonetheless, whatever misalignment occurs in practice during the mechanical assembly can be accurately corrected for by a calibration with monochromatic beams reflected from a reference crystal positioned at the sample position.

For a single HOPG analyzer crystal with a mosaic FWHM of  $0.5^\circ$ , the fractional wavelength resolution  $\delta\lambda/\lambda$  is of the order of 0.01 for an incident beam of 5 Å nominal wavelength and an angular divergence of several minutes of arc. This resolution is typical for a conventional neutron reflectometer employing a quasi-monochromatic beam at a continuous source [5]. In the conceptual design of the energy-dispersive detector array for application in a polychromatic beam reflectometer, such as the CANDOR instrument at the NCNR, comparable wavelength resolution could be maintained by spacing the successive HOPG crystals at angular increments of about one degree (for HOPG with  $0.5^\circ$  FWHM mosaic) so that no appreciable wavelength bandwidth overlap would occur.

As it happens, for the majority of specular neutron reflectivity measurements performed on sample systems under investigation, data can be collected with a useful signal-to-noise out to a wavevector transfer  $Q$  of about to only  $0.5 \text{ \AA}^{-1}$  — over this range a fractional wavelength resolution of 0.01 can be relaxed by a factor of two or more without significantly degrading the  $Q$  resolution. Consequently, the angular incremental change in angles between successive HOPG crystals for the energy-dispersive detector described herein has been selected to be  $0.5^\circ$ . Thus, some overlap of the wavelength ranges diffracted by

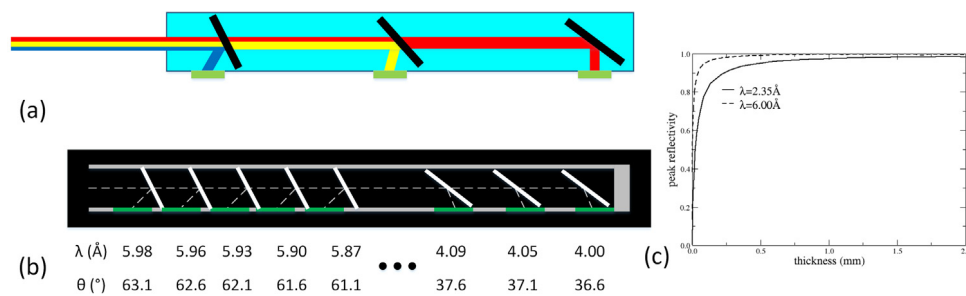


Fig. 2. (a) Schematic concept for energy dispersive neutron detection where the diffracted polychromatic beam passes through a series of analyzer crystals. The analyzers are set to select a single wavelength from the beam with high reflectivity but low absorption of the shorter wavelength neutrons which will continue down the channel. (b) Details of a single analyzer/detector channel, showing the arrangement of each PG analyzer crystal (white) and scintillation detector (green). (c) Calculated reflectivity as a function of analyzer thickness, showing  $>90\%$  reflectivity for neutrons in the bandwidth of interest [3].

adjacent crystals occurs, thereby resulting in an intentionally relaxed wavelength resolution for the instrument. However, the number of neutrons reflected by a sample which can be usefully analyzed is correspondingly increased by a factor of two.

### 3. Neutron detectors

For decades, the detector of choice at neutron scattering facilities worldwide has been the  $^3\text{He}$  gas-filled proportional counter [6]. These tubes combine the desired features of tunable neutron absorption, high detection efficiency, and excellent neutron–gamma discrimination. For a single array of the type described above, the  $^3\text{He}$  proportional counter would be an ideal neutron sensor. However, if the neutron detector is exceedingly thin ( $<2$  mm), it would be possible to pack many energy-analyzing arrays side by side to increase the solid angle of detection of any spectrometer using them. This is particularly important for specular scattering measurements in which angularly divergent incident beams are employed and the reflectivity of the sample varies by several orders of magnitude over the angular range covered. The efficiency of a reflectometer or diffractometer is also maximized for non-specular scattering by packing multiple arrays of such detectors together over the minimum angular range possible.

Neutron sensitive scintillators have been used for more than twenty years in neutron scattering instrumentation, forming the basis of many different variations of position sensitive neutron detectors [7–10]. Screens of the venerable scintillator  $^6\text{LiF:ZnS(Ag)}$  have been read out with both clear and wavelength shifting (WLS) fibers running to photomultipliers. The basic principle of operation is one in which incident neutrons are captured by the highly absorbing  $^6\text{LiF}$ , liberating a proton and triton with 4.8 MeV kinetic energy. The reaction products excite the  $\text{ZnS(Ag)}$  phosphor, which decays back to its ground state with the emission of 450 nm (blue) photons. Some of those photons are captured by the K-27 dye in the WLS fiber and reemitted as 476 nm (green) photons which then travel to the photosensor.

Although the photon yield from a neutron capture is quite large (nominally 160,000 photons per neutron capture), a number of factors (opacity of  $\text{ZnS}$  to its own scintillation light, losses encountered in photon transport, photodetection efficiency of the photosensor) conspire to reduce the signal to a tiny level. Further, the inherent gamma sensitivity of the scintillator and thermally induced avalanches in the photosensor make neutron discrimination a challenging proposition.

GEANT4 simulations of this system have already pointed to several important optimizations to be made in the grain size and stoichiometry of  $^6\text{LiF}$  and  $\text{ZnS}$  in the scintillator and the arrangement and placement of the WLS fibers in the scintillator [11,12].

In our design, wavelength shifting fibers are laid side by side in a frame and a layered structure of scintillator materials is formed around the fibers, starting with an alcohol-soluble mixture of  $^6\text{LiF}$  neutron converter, nickel-doped  $\text{ZnS(Ag)}$  phosphor, and an inert binder. For simplicity's sake, we refer to the scintillator according to weight ratios of these three principle components. Once this “primer” layer (1:2:0.6) is applied, slabs of 1:2:0.14 scintillator backed by optical reflectors are pressed around the material so that the WLS fibers are completely embedded in scintillator. To encourage modularity of design, a single frame holds three separate detectors (Fig. 3).

0.5 mm WLS fibers (Kuraray Y-11, with 650 ppm of K-27 dye [13]) are terminated, polished, and butted on one end into a mirrored aluminum reflector. The other end is bundled into a  $2.7\text{ mm} \times 2.7\text{ mm}$  area in an aluminum block. The fibers are then cut with a hot knife and polished down to the face of the block.

A printed circuit board holding the silicon photomultipliers ( $3\text{ mm} \times 3\text{ mm}$  active area) fastens to the top of the fiber block and registers the silicon photomultipliers with the polished fiber ends.

A fully assembled array including HOPG crystals, neutron detectors, and preamplifiers is shown in Fig. 4.

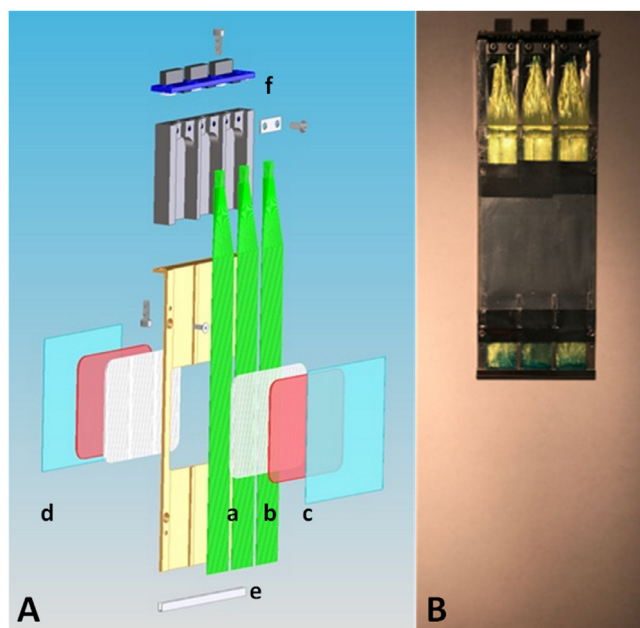


**Fig. 3.** Exploded assembly diagram (A) and photograph (B) of the triple frame neutron detector. Layer “a” consists of a 1:2:0.6 Ni-doped scintillator “primer”. Layer “b” is a slab of 1:2:0.14  $\text{LiF:ZnS}$ :binder scintillator. Layer “c” is the Alanod reflector on the leading face. Layer “d” is the Vikuiti reflector on the trailing face. A terminal reflector (e) is attached to the bottom of the frame. The SiPMs are mounted on a carrier board mating to the WLS fibers (f).

### 4. Electronics

Most current applications of neutron scintillator technology make use of traditional photomultipliers as a photosensor. We have selected silicon photomultipliers as the photosensor for their compact size, low cost, and insensitivity to magnetic fields. These sensors, however, also present some challenges as they have some amount of inherent thermal noise, delayed crosstalk, and afterpulsing which can affect the interpretation of the signal.

Having studied several candidate devices, we selected the commercial SensL J series SiPM in the  $3\text{ mm} \times 3\text{ mm}$  surface mount package [14,15]. This SiPM has low dark current ( $45\text{ kHz/mm}^2$ ) and high photodetection efficiency ( $>50\%$  at 420 nm) at a low breakdown voltage (24.5 V). We operated at 2 V above the breakdown. The J-series SiPM also has a short recovery time, which improves the ability to distinguish gamma and neutron events.

A custom preamplifier board distributes the negative bias voltage to the SiPMs and provides two stages of amplification to adjust signal gains. The configuration was designed for high bandwidth and positive going output signals. As the SiPMs are grouped in threes to mount to the triple frame scintillators, each preamplifier board takes signals from six triples frames for a total of eighteen parallel outputs. The circuits were implemented with surface mount components to minimized electromagnetic interference noise susceptibility and to ensure that the gains are stable at high frequencies.

Fig. 5 shows typical waveforms from the preamplified SiPM signal illustrating different types of events. Because the intensity of the signal for neutron and gamma events can be similar, pulse height discrimination techniques are insufficient to discriminate neutron events from other signal types. Pulse shape discrimination is much more sensitive as it can better differentiate the signal types based on the decay of the waveform. In our studies, we used a pulse shape discrimination technique using two integration windows: a prompt integration window, typically less than 200 ns, and a delayed (or tail) integration window, typically greater than 1500 ns [16].

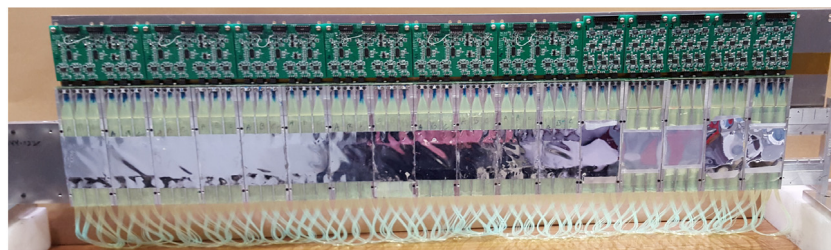


Fig. 4. Complete assembled array of HOPG crystals with scintillator neutron detectors and preamplifiers mounted.

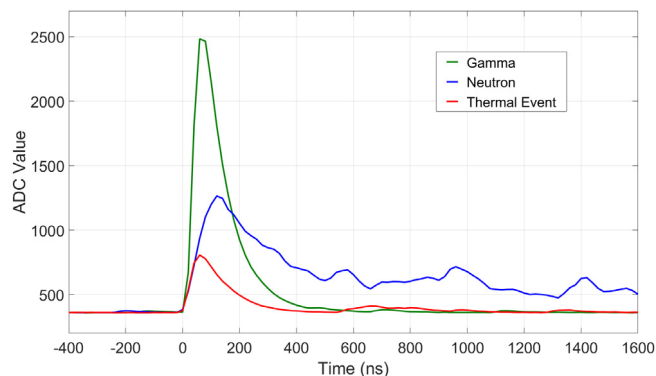


Fig. 5. Waveforms from the SiPM illustrating the typical signatures of neutron and gamma capture events alongside thermal noise. Gamma capture and thermal noise events are typically very short in duration ( $<200$  ns) whilst neutron capture events can persist for many microseconds.

The raw signal from the SiPM is digitized using a high-speed digitizer (50 MS/s). A field programmable gate array monitors the digitized signal and applies the two-window discrimination algorithm in real time to filter out candidate events. Neutron events are tagged with a timestamp and are read out by an application for histogramming.

## 5. Experimental

Characterizations of the scintillator neutron detector were conducted on the Polarized Helium and Detector Experiment Station (PHADES) spectrometer on guide NG7 at the NIST Center for Neutron Research [17]. The PHADES instrument uses a HOPG monochromator crystal set at a fixed angle to provide a monochromatic beam of  $4.1 \text{ \AA}$  (4.86 meV) neutrons with a neutron flux of  $2 \times 10^6 \text{ cm}^{-2} \text{ s}^{-1}$ . Transmission measurements were made with the use of a  $^3\text{He}$  proportional counter confirmed to have 94% sensitivity to neutrons at  $5 \text{ \AA}$ .

Characterizations of the detector array were performed on the Spin Polarized Triple Axis Spectrometer (SPINS) on guide NG5 at the NIST Center for Neutron Research [18]. The SPINS spectrometer uses a HOPG (002) monochromator to direct a monochromatic beam of  $2.4 \text{ \AA}$  (2.4 meV) to  $5.84 \text{ \AA}$  (14 meV) neutrons towards a sample under test.

The instrumental wavelength resolution can be determined by a direct series of measurements employing well collimated and nearly monochromatic beams incident on each crystal in the array, one at a time. This can be accomplished by mounting the array on a two-axis neutron diffractometer (such as the one at PHADES or SPINS) in an inverse geometry such that the incident beam is along the direction of the Bragg reflected beam into its corresponding scintillator detector plate, but with the direction reversed and the plate removed. The crystal can then be rocked about an axis normal to the scattering plan (defined by the incident and reflected neutron wavevectors) and the change in the transmitted intensity through the crystal measured as a function of that angle. In this manner, the actual effective angular distribution of

each HOPG crystal can be characterized independently of the upstream crystals in the array.

For characterizations of the array performance, the array was placed on the sample table of the spectrometer and aligned along the incident beam direction. The primary spectrometer was then scanned from low to high energy and neutron events processed over the entire array. The expected result is that the intensity at each point should peak in the detector channel associated with the same nominal neutron final energy.

Combining the information obtained for each individual crystal thereby obtained with its measured behavior in the normal configuration with the upstream crystals in place, the effective wavelength resolution for the energy-dispersive of the entire array can be accurately determined for use in numerically deconvoluting the instrumental resolution from scattering data obtained for a sample under investigation.

## 6. Performance

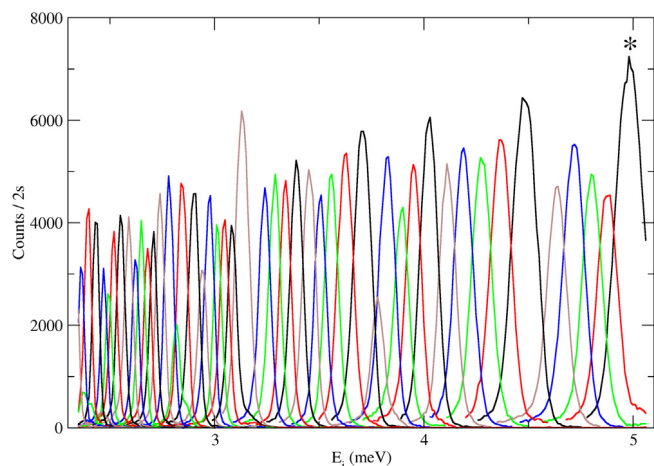
Working iteratively to tune the mechanical parameters and composition and arrangement of scintillator materials we have been able to reproducibly manufacture scintillator based proportional counters exhibiting  $74.1\% \pm 0.9\%$  [73.8,74.3] absolute sensitivity for  $4.1 \text{ \AA}$  (4.86 meV) neutrons ( $90.3\% \pm 1.1\%$  [90.0,90.6] for  $5.0 \text{ \AA}$  neutrons). This result was confirmed using both gold foil activation measurements and calibrated fluence monitors. Pulse shape discrimination has enabled excellent gamma rejection ( $2 \times 10^{-7}$ ), confirmed using isotopic  $^{60}\text{Co}$  and  $^{137}\text{Cs}$  sources. Count rate studies have shown that the counters are capable of handling neutron captures at sustained rates of 10 kHz.

Fig. 6 shows the processed data for the test described in Section 5, normalized to the incident beam flux. The peaks in the figure are the traces from each individual neutron detector channel and coincide with the nominal final energy of each analyzer crystal. In the figure, the peak marked with an asterisk coincides with the first analyzer crystal in the array. As can be seen the general trend is for the intensity in successive energy channels to decrease.

The lineshapes of each peak are mostly Gaussian with  $\text{FWHM} = 0.7200^\circ \pm 0.0012^\circ$ . We observe that many of the peaks are asymmetric, but that this is not systematic. Ideally the mosaic distribute of an HOPG crystal would be Gaussian with a well-defined FWHM. In practice, however, deviations from a symmetric Gaussian mosaic distribution may occur in the manufacturing process or by mechanical deformation of the crystal in clamping devices. The shape of the mosaic distribution may also appear distorted if during measurement with neutrons of a particular incident wavelength and at the proper angle there is an inelastic scattering contribution from phonon excitations in the crystal, especially in the neighborhood of the [002] reflection employed for wavelength selection by Bragg diffraction.

## 7. Signal to noise in crystal analyzers

Although pyrolytic graphite is an almost ideal crystal monochromator for slow neutrons (from  $1 \text{ \AA}$  to  $6 \text{ \AA}$  in wavelength) with nearly zero absorption or incoherent scattering cross sections, it does possess a relatively small thermal diffuse scattering (TDS) cross section associated with inelastic scattering from phonon excitations. While the coherent



**Fig. 6.** Processed data from a test of the full array on a neutron triple axis spectrometer. The array is mounted on the downstream end of the monochromator drum such that the exiting beam runs down the center of the array. As the monochromated beam matches the nominal energy of a given HOPG crystal, the signal in its associated neutron counter is maximized. Each peak in this figure corresponds to the nominal energy of one of the HOPG crystals. The peak marked with an asterisk corresponds to the first analyzer crystal in the array.

elastic scattering that gives rise to the Bragg reflection process – used to monochromate neutron beams – is predominant, TDS at room temperature can contribute of the order of half a percent of the scattering that takes place in each of the crystals of the thickness that we are employing in the energy-dispersive detector. Typically, this relatively small amount of TDS is not problematical in many scattering instruments using HOPG. In an application such as specular reflectometry, however, under certain circumstances the amount of TDS that is produced by some fraction of the upstream analyzers of the array when a polychromatic beam enters the detector can produce a less than optimal signal-to-noise ratio in a corresponding, adjacent scintillation detector (i.e., the number of elastically Bragg reflected neutrons of the primary wavelength – the signal – divided by neutrons of all wavelengths present scattered by TDS). Measurements of the transmission of neutrons through a well-defined thickness of HOPG at room temperature show that the fraction of TDS in a one mm thick section is of the order of 0.005 at a single wavelength of 5 Å [19]. Given the more isotropic character of the TDS scattering compared to the highly directional elastic Bragg scattering, and taking into account the solid angle viewed by a detector plate adjacent to its corresponding analyzer crystal, the signal-to-noise ratio to be expected can be estimated. For example, consider the case of a continuous range of wavelengths of uniform intensity between 4 Å and 6 Å entering the detector. At the position of the first, upstream crystal, the ratio of Bragg reflected intensity of 6 Å neutrons divided by the TDS entering the immediately adjacent detector plate is approximately 20 at room temperature (for a Bragg reflectivity of 0.995 and a TDS reflectivity of 0.005). On the other hand, at the last or 54th crystal on the downstream end of the array, where most of the neutrons have been already reflected out by their appropriate upstream analyzer crystals, the signal-to-noise ratio for the nominal 4 Å neutron detector would be approximately 750 at room temperature. (This calculation takes into account the loss of neutrons by both Bragg and TDS scattering as the beam propagated through the array.) Although at first thought such signal-to-noise ratios do not necessarily appear to be an issue, it becomes more problematical when scattering from a sample for which the distribution of reflected neutrons is not known *a priori* and the signal is much weaker, relatively, at a particular wavelength.

Fortunately, the relationship between neutrons reflected by Bragg and TDS processes can be described by a simultaneous system of linear

algebraic equations which can be solved to separate out the desired signals from the TDS background for any scattering distribution produced by an arbitrary sample being investigated on a scattering instrument using such a wavelength-dependent detector array. The intensity  $D_j$  collected by the  $J_{th}$  detector (adjacent to the  $J_{th}$  analyzer crystal) can be expressed as

$$D_j = I_{\lambda_j} R(\theta, \lambda_j) (1 - r_{TDS})^{J-1} [r_{BRAGG} - (1 - f)r_{TDS} + fr_{TDS}] + J \sum_{K=1}^{J-1} I_{\lambda_K} R(\theta, \lambda_K) (1 - r_{TDS})^{K-1} \times (1 - r_{BRAGG}) fr_{TDS} + N \sum_{K=J+1} I_{\lambda_K} R(\theta, \lambda_K) (1 - r_{TDS})^{K-1} fr_{TDS} \quad (1)$$

where  $I_{\lambda_j}$  is the intensity of neutrons of wavelength  $\lambda_K$  incident on a sample,  $R(\theta, \lambda_j)$  is the reflectivity of that sample at a particular scattering angle  $2\theta$  and for a specific wavelength  $\lambda_j$ ,  $(1 - r_{TDS})^{J-1}$  represents the product probability that neutrons are transmitted through  $J - 1$  preceding HOPG analyzer pieces without being scattered out via TDS (reflection probability  $r_{TDS}$ ) and which can, therefore, reach the  $J_{th}$  crystal and its adjacent detector plate,  $f$  is the fraction of solid angle of acceptance in the detector plate for TDS scattering from the adjacent HOPG crystal, and  $r_{BRAGG}$  is the reflectivity for Bragg scattering from the crystal into the neighboring detector plate. In Eq. (1) it has been implicitly assumed that the Bragg reflectivity is essentially equivalent for all crystals at all wavelengths between 4 Å and 6 Å wavelength and that the TDS scattering is essentially the same over this wavelength range for the purposes of providing a simpler expression as an illustration. If in practice  $r_{TDS}$  and/or  $r_{BRAGG}$  are in fact wavelength dependent, then the appropriate values can be substituted without changing the essential underlying mathematical formulation. In actual practice,  $r_{TDS}$ ,  $r_{BRAGG}$ , and  $f$  are quantities which can be determined independently on the instrument using the direct incident polychromatic beam (without a scattering sample present) and by appropriate measurements with a reference crystal monochromator at the sample position and properly oriented to reflect each of the constituent quasi-monochromatic wavelength bands one at a time. The intensities incident on the sample,  $I_{\lambda_j}$ , can also be determined *in situ* on the scattering instrument in similar fashion. Furthermore, in the derivation of the above expression for the intensity incident on a detector in the array, it is presumed that the  $J_{th}$  detector receives through the Bragg process only wavelengths within the narrow range defined by the crystal mosaic, i.e., of the order of 0.01 fractional wavelength resolution. In practice, however, more overlap can be intentionally imposed in the design to optimize efficiency — in such case the equations presented above would have to be modified accordingly, though this is straightforward and also does not change the essential formulation of the mathematical description. Thus, the  $J_{th}$  detector is associated with the  $J_{th}$  wavelength band about  $\lambda_j$  only. Likewise, the TDS scattering background is taken to originate solely from the crystal immediately adjacent from a given detector — any significant contributions from other crystals in the neighborhood can be accounted for in a straight forward manner as necessary.

Now there are  $N$  detectors and  $N$  corresponding narrow wavelength bands (where for the detector being described in this report  $N$  is 54) so that Equation E1 can be used to form a system of  $N$  related linear algebraic equations such that simultaneous solution gives *a priori* unknown quantities describing the sample being investigated, namely the reflectivities  $R(\theta, \lambda_j)$ . Rearranging the terms in Eq. (1), we can write

$$\begin{aligned} D_1 &= C_{11} R(\theta, \lambda_1) + C_{12} R(\theta, \lambda_2) + C_{13} R(\theta, \lambda_3) + \dots + C_{1N} R(\theta, \lambda_N) \\ D_2 &= C_{21} R(\theta, \lambda_1) + C_{22} R(\theta, \lambda_2) + C_{23} R(\theta, \lambda_3) + \dots + C_{2N} R(\theta, \lambda_N) \\ D_3 &= C_{31} R(\theta, \lambda_1) + C_{32} R(\theta, \lambda_2) + C_{33} R(\theta, \lambda_3) + \dots + C_{3N} R(\theta, \lambda_N) \\ &\vdots \\ D_N &= C_{N1} R(\theta, \lambda_1) + C_{N2} R(\theta, \lambda_2) + C_{N3} R(\theta, \lambda_3) + \dots + C_{NN} R(\theta, \lambda_N) \end{aligned} \quad (2)$$

where

$$C_{JJ} = \left\{ I_{\lambda J} (1 - r_{TDS})^{J-1} [r_{BRAGG} - (1 - f)r_{TDS} + fr_{TDS}] + I_{\lambda J} (1 - r_{TDS})^{J-1} (1 - r_{BRAGG}) fr_{TDS} \right\}$$

and

$$C_{JK} = I_{\lambda K} (1 - r_{TDS})^{K-1} (1 - r_{BRAGG}) fr_{TDS} \text{ (for } K < J)$$

and

$$C_{JK} = I_{\lambda K} (1 - r_{TDS})^{K-1} fr_{TDS} \text{ (for } K > J).$$

In general, the system of linear equations represented by Eq. (2) can be rewritten as

$$\begin{bmatrix} C_{11} & C_{12} & C_{13} & & C_{1N} \\ C_{21} & C_{22} & C_{23} & & C_{2N} \\ C_{31} & C_{32} & C_{33} & & C_{3N} \\ & & & \ddots & \vdots \\ C_{N1} & C_{N2} & C_{N3} & \dots & C_{NN} \end{bmatrix} \begin{bmatrix} R(\theta, \lambda_1) \\ R(\theta, \lambda_2) \\ R(\theta, \lambda_3) \\ \vdots \\ R(\theta, \lambda_N) \end{bmatrix} = \begin{bmatrix} D_1 \\ D_2 \\ D_3 \\ \vdots \\ D_N \end{bmatrix}. \quad (3)$$

In the case in which  $r_{TDS} = 0$ , Eq. (3) reduces to

$$\begin{bmatrix} C_{11} & 0 & 0 & & 0 \\ 0 & C_{22} & 0 & & 0 \\ 0 & 0 & C_{33} & & 0 \\ & & & \ddots & \vdots \\ 0 & 0 & 0 & \dots & C_{NN} \end{bmatrix} \begin{bmatrix} R(\theta, \lambda_1) \\ R(\theta, \lambda_2) \\ R(\theta, \lambda_3) \\ \vdots \\ R(\theta, \lambda_N) \end{bmatrix} = \begin{bmatrix} D_1 \\ D_2 \\ D_3 \\ \vdots \\ D_N \end{bmatrix} \quad (4)$$

so that there is a simple solution for the  $R(\theta, \lambda_j)$  independent of all the other sample reflectivity values.

From an experimental measurement viewpoint, given statistical uncertainty and the propagation of error which accompanies the solution of the above system of equations, it is advantageous to have a value of  $r_{TDS}$  as close to zero as possible.

One demonstrated way to markedly reduce the TDS is to cool the HOPG crystals to temperatures approaching absolute zero [20]. In neutron scattering instruments such as backscattering spectrometers, it has been demonstrated that cooling HOPG to temperatures of about 25 Kelvin result in a decrease in the background due to TDS by a factor of 12 and perhaps as much as a factor of 48 at 5 Kelvin [20]. This occurs because the TDS scattering associated with phonon creation and annihilation decreases nearly linearly with decreasing temperature in pyrolytic graphite. For the application of the energy-dispersive detector described in this paper to the CANDOR instrument under construction at the NCNR, the plan is to cool the HOPG to below 10 Kelvin using closed cycle refrigerators (CCRs).

Another way to significantly reduce the TDS background is to reduce the thickness of the HOPG analyzer crystals (at the 4 Å to 6 Å wavelength range utilized in the present device, a reduction of thickness by a factor of two, from 1.0 mm to 0.5 mm, would reduce the crystal peak reflectivity by only a few percent). It has been shown, incidentally, that monochromator grade HOPG can be cleaved accurately parallel to the reflecting (002) planes without significant degradation of its neutron peak reflectivity or broadening of its mosaic FWHM [21].

## 8. Summary

We describe the concept, design, refinement, and construction of an energy dispersive detector for cold neutrons. The detector consists of a sequential array of highly oriented pyrolytic graphite crystals set at 54 successive angles corresponding to neutron kinetic energies between 2.29 meV and 5.11 meV. Neutrons entering the 10 mm wide × 30 mm tall channel of the detector will be diffracted by the analyzer crystals into an associated neutron proportional counter.

The scintillator based neutron detectors developed as part of this project have performance characteristics of the ubiquitous  $^3\text{He}$  gas filled tubes in a thickness less than 2 mm. The calibrated sensitivity was 93% ± 1% for 4.86 meV (4.1 Å) neutrons. The gamma rejection ratio was

on the order of  $2 \times 10^{-7}$  and the counter could be operated at rates exceeding 10 kHz without deadtime correction.

We constructed a room temperature prototype array outfitted with scintillator based neutron detectors, SiPMs, preamps, and digitizers. The room temperature array performed essentially as intended on a cold neutron triple axis instrument, with the intensity of detected radiation peaking in the channels associated with the correct energy bin thereby validating the principle of operation. We believe that this energy dispersive detector could enable many potential applications, including rapid measurements in reflectometry and diffractometry using polychromatic beams, highly parallel triple axis measurements, and time resolved studies of many kinds of materials.

Recognizing that the thermal diffuse background associated with the HOPG analyzer crystals could dramatically impair the ability of this detector to operate over the nearly 8 decades of dynamic range required for applications like white beam reflectivity and measurements of material dynamics, we have embarked on a project to cryogenically cool the graphite. Cryogenically cooled arrays will form the basis of the CANDOR instrument when it is commissioned.

## 9. Disclaimer

Certain trade names and company products are identified to adequately specify the experimental procedure. In no case does such identification imply recommendation or endorsement by the National Institute of Standards and Technology, nor does it imply that the products are necessarily the best for the purpose.

## References

- [1] <http://www.ncnr.nist.gov/instruments/CANDOR>, [Online].
- [2] A.H. Venkatesh, K.R. Rao, A simple white beam neutron diffraction technique, *Pramana* 8 (2) (1977) 184–204.
- [3] J.M. Simmons, J.C. Cook, R.M. Ibberson, C.F. Majkrzak, D.A. Neumann, Polychromatic energy dispersive neutron diffraction at a continuous source, *J. Appl. Crystallogr.* 46 (2013) 1347–1352.
- [4] D. Mildner, M. Arif, S.A. Werner, Neutron transmission through pyrolytic graphite monochromators, *J. Appl. Crystallogr.* (2001) 258–262.
- [5] J.A. Dura, D.J. Pierce, C.F. Majkrzak, N.C. Maliszewskyj, D.J. McGillivray, M. Loesche, K. O'Donovan, M. Mihailescu, U. Perez-Salas, D. Worcester, S. White, AND/R: Advanced neutron diffractometer/reflectometer for investigation of thin films and multilayers for the life sciences, *Rev. Sci. Instrum.* 77 (2006) 074301.
- [6] G.F. Knoll, *Radiation Detection and Measurement*, John Wiley and Sons, New York, 1999.
- [7] N.J. Rhodes, M.W. Johnson, C.W. Van Eijk, The future of scintillator detectors in neutron scattering instrumentation, *J. Neutron Res.* 4 (1996) 129–133.
- [8] N.J. Rhodes, Scintillation detectors, *Neutron News* (2012) 26–30.
- [9] D.P. Hutchinson, R.K. Richards, D.E. Holcomb, J.A. Ramsey, Position sensitive neutron detectors using a crossed fiber readout array, *Proc. SPIE* 3769 (1999).
- [10] J.B. Mosset, A. Stoykov, U. Greuter, M. Hildebrandt, N. Schlumpf, H. Van Swygenhoven, Evaluate of two thermal neutron detection units consisting of ZnS/6LiF scintillating layers with embedded WLS fibers read out with a SiPM, *Nucl. Instrum. Methods A* 764 (2014) 299–304.
- [11] Y. Yehuda-Zada, K. Pritchard, J.B. Ziegler, C. Cooksey, K. Siebein, M. Jackson, C. Hurlbut, Y. Kadmon, Y. Cohen, R.M. Ibberson, C.F. Majkrzak, N.C. Maliszewskyj, I. Orion, A. Osovizky, Optimization of 6LiF:ZnS(Ag) scintillator light yield using GEANT4, *Nucl. Instrum. Methods A* 892 (2018) 59–69.
- [12] A. Osovizky, K. Pritchard, Y. Yehuda-Zada, J. Ziegler, E. Binkley, P. Tsai, A. Thompson, N. Hadad, M. Jackson, C. Hurlbut, G. Baltic, C.F. Majkrzak, N.C. Maliszewskyj, Design of an ultrathin cold neutron detector, *Nucl. Instrum. Methods A* 893 (2018) 1–9.
- [13] Kuraray, Japan, <http://hallweb.jlab.org/experiment/PVDIS/SoLID/EC/meetings/kuraray/Absorption&Emission%20of%20Y7811-1.pdf>, [Online].
- [14] A. Osovizky, K. Pritchard, Y. Yehuda-Zada, J.B. Ziegler, P. Tsai, M. Ghelman, A.K. Thompson, R.M. Ibberson, G.M. Baltic, C.F. Majkrzak, N.C. Maliszewskyj, Selection of silicon photomultipliers for a 6LiF:ZnS(Ag) scintillator based neutron detector, *J. Phys. Comm.* 2 (4) (2018) 045009.
- [15] SensL, Ireland, J-Series Family, [Online].
- [16] K.M. Pritchard, A.N. Osovizky, J.B. Ziegler, E. Binkley, P. Tsai, N. Hadad, M. Jackson, C. Hurlbut, G.M. Baltic, C.F. Majkrzak, N.C. Maliszewskyj, Computational Techniques for Optimizing Performance in a LiF:ZnS(Ag) Neutron Detector Using Recorded Waveforms. in preparation.

- [17] R. Erwin, K. Krycka, S. Watson, PHADES, 2017. [Online]. Available: <http://www.ncnr.nist.gov/instruments/instdev.html>.
- [18] L. Harriger, Spin Polarized Inelastic Neutron Spectrometer, 2017. [Online]. Available: <http://www.ncnr.nist.gov/instruments/spins>.
- [19] J.C. Cook, personal communication.
- [20] C.J. Carlile, M.A. Adams, P. Krishna, M. Prager, K. Shibata, P. Westerhuijs, Less background, better contrast by cooling analyzer crystals, *Nucl. Instrum. Methods A* 338 (1994) 78–82.
- [21] A.K. Freund, D.H. Yu, Optimization and fabrication of a composite pyrolytic graphite monochromator for the Pelican instrument at the ANSTO OPAL reactor, *Nucl. Instrum. Methods A* 634 (2011) S75–S80.